Acoustic Meta-Equalizer

Yifan Zhu,* Shi-Wang Fan, Liyun Cao, Krupali Donda, and Badreddine Assouar†
Institut Jean Lamour, CNRS, Université de Lorraine, 54000 Nancy, France

(Received 19 February 2020; revised 26 May 2020; accepted 24 June 2020; published 14 July 2020)

Acoustic equalization is the process of adjusting the frequency response of a broadband sound signal, which is widely used in communication-system and audio acoustics. Here we introduce the concept of an acoustic meta-equalizer, viz., a passive acoustic metamaterial-based filter that has a tunable frequency response within an ultrabroadband range (200 Hz–20 000 Hz) and is capable of generating a frequency equalization on the input sound signal. By using two kinds of acoustic resonant elements, viz., Helmholtz and Fabry-Perot resonators, we realize and demonstrate ultrabroadband and tunable filters within an integrated meta-structure. In analogy with the conventional equalizer concept in signal processing, we numerically, analytically, and experimentally demonstrate functional filters, signal reproductions, and sound-effect controls by the conceived acoustic meta-equalizer.

DOI: 10.1103/PhysRevApplied.14.014038

I. INTRODUCTION

Equalization is an important concept in signal processing; that is, adjusting the frequency response of a broadband signal. It has been and still is widely used in telecommunications [1–3] and various acoustic applications, including audio devices [3–5], room acoustics [6–10], and underwater communications [11,12]. The resulting filter device is known as an equalizer (EQ). The acoustic equalizer device can adjust the loudness curve of a broadband sound signal to improve the quality of audio sound, because the tone color of sound is influenced by different frequency ingredients [4,5]. In room acoustics [6–8], different complex acoustic environments will influence the uniformity of the frequency response, so acoustic equalization can be used to reproduce the sound signals [6–8] or to realize active noise control [9,10]. In hydroacoustics, similarly, the complex environment makes the acoustic equalization process necessary in underwater acoustic communications [11,12].

On the other hand, during the last decade, acoustic metamaterials have been actively studied [13,14], providing different design strategies for various acoustic devices. For example, acoustic metamaterials have been proposed to actively control specific interesting acoustic phenomena, such as the cocktail effect [15], acoustic reverberation [16], and an acoustic hologram [17]. Acoustic metamaterials are also used for underwater communications [18,19]. For the design of sound absorbers, acoustic metamaterials can bring real added value to the absorption performance with large bandwidth and reduced sample thickness [20]. To further decrease the thickness of acoustic resonant units, the concept of acoustic metasurfaces was proposed [21] to design unconventional ultrathin acoustic devices. For instance, a metasurface-based Schroeder-diffuser design [22] is only one tenth the thickness of conventional designs [23]. For a sound absorber, a deep-subwavelength metasurface-based absorber was evidenced [24], which is much thinner than the absorber from classical materials, showing the great flexibility and potential of acoustic metamaterials and metasurfaces.

In this research, we extend the general concept of acoustic metamaterials to an equalizer by proposing the concept of an acoustic meta-equalizer (AMEQ), viz., a tunable and ultrabroadband passive acoustic metamaterial filter. Previous designs of acoustic filters [25–28] have shown limited bandwidth (narrowband) or limited amplitudes (only 0 and 1). Therefore, an ultrabroadband and tunable acoustic filter is highly desired for practical acoustic applications. In our proposed concept, the designed AMEQ can realize different specific amplitude controls with different values (−2 to −10 dB, with a step of −2 dB) within an ultrabroadband range (200–20 000 Hz). This design goal is realized by our using two kinds of acoustic resonant elements, viz., Helmholtz resonators (HRs) [29,30] and Fabry-Perot resonators (FPRs); that is, an array of narrow tubes with different depths [20,31]. We realize both low-frequency equalization and high-frequency equalization with these two acoustic elements, respectively, in an integrated acoustic metastructure. Although these acoustic resonant elements have been demonstrated for sound absorption [20,31,32] before, realizing an ultrabroadband filter is challenging due to the very large span of the targeted frequencies (seven octaves). This makes the size of the whole structure subwavelength for low frequencies, but

*yifan.zhu@univ-lorraine.fr
†badreddine.assouar@univ-lorraine.fr

larger than the wavelength for high frequencies. Therefore, the low-frequency filters are due to the coupled resonance of the whole structure, while the high-frequency filters are determined by both the resonance of FPRs and the geometric acoustic effect. This complex case requires deliberate design (including the geometric feature of the channel and the size and position of each resonator). It is distinct from conventional acoustic absorber designs, which is demonstrated numerically, analytically, and experimentally in the following sections.

We illustrate in Fig. 1 the classical EQ concept in different application domains. Figure 1(a) shows an audio EQ device, which is widely used in sound-effect manipulations. Figure 1(b) shows the EQ software, which can change the sound-frequency ingredients of an audio signal on a computer. The amplitude response of different frequencies can be freely modulated within a specific range. Figure 1(c) shows that underwater communications rely on the frequency-equalization process since the complex hydroacoustic environment needs frequency-ingredient correction. Our proposed acoustic meta-equalizer is shown in Fig. 1(d). It consists of an acoustic metamaterial with several modulators. The latter are designed for specific amplitude control at different frequencies. By geometrically optimizing the metamaterial frame size and the parameters of HRs and FPRs, we can achieve highly precise manipulation of the transmission coefficient for each octave. An integrated physical model is proposed to calculate the transmission for low and high frequencies, respectively. The corresponding analytical results agree well with the simulated and measured ones. Here, in analogy with a conventional EQ device, we show the realization of different functional filters, signal reproduction, and the modulation of specific sound effects by the AMEQ. Our findings integrating multiple functionalities will lead to real-world applications of acoustic metamaterials in room acoustics and architectural acoustics.

II. RESULTS

A. Metastructure design and analytical model

The conceived AMEQ is a two-port structure as schematically shown in Fig. 2(a). The acoustic wave is incident from one port and transmitted to another port as the arrows indicate. The whole structure can be regarded as a "black box" with frequency-equalization function. The two-dimensional (2D) structure is designed as a furcate channel with several modulators on both sides of the channel. The main difficulty and challenge for AMEQ design is that the modulators should cover distinctly different resonant frequencies within an ultrabroadband range. Inspired by previous work, such as acoustic absorber and diffuser

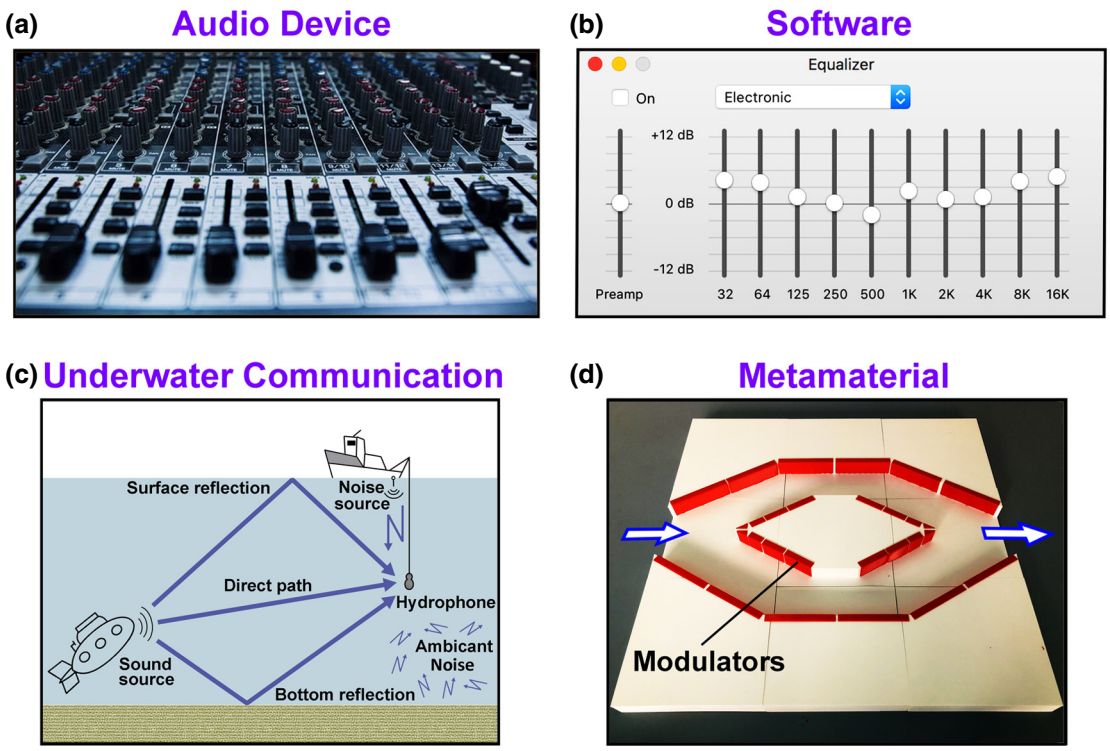

FIG. 1. The concept of an equalizer with different potential applications. (a) EQ device in audio acoustics. (b) EQ software for sound-effect control on a computer. (c) Underwater acoustic communication relies on an acoustic frequency equalization process. (d) Photograph of the AMEQ, which is an acoustic metamaterial panel with several modulators.

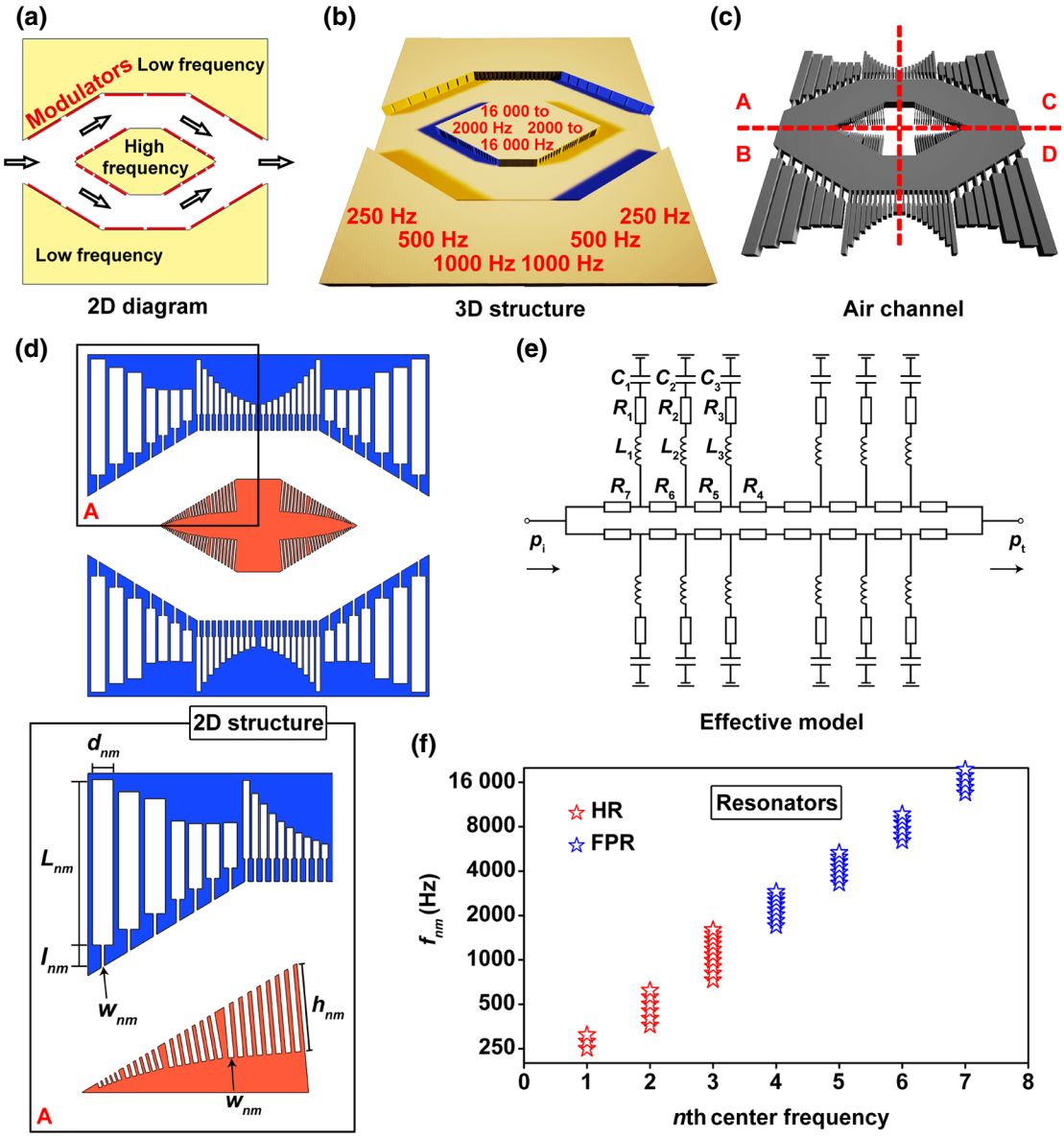

FIG. 2. The AMEQ. (a) The AMEQ device composed of a 2D channel structure with several modulators on both sides of the waveguide. The modulators for high and low frequencies are marked. The arrows indicate the transmission directions. (b) Three-dimensional structure of the AMEQ. The filters for the different center frequencies are marked. (c) The 3D structure of the air channel in which the sound is transmitted. The whole structure is symmetrical in the four quadrants marked by *A*, *B*, *C*, and *D*. (d) Two-dimensional structure of the AMEQ. The box at the bottom shows an enlarged view of the solid box, showing a structural schematic diagram of the unit cell, with different geometric parameters marked in the figure. (e) The effective-circuit model of the AMEQ. The arrows indicate the input and output ports. (f) The optimized resonant-frequency f_{nm} distributions of HRs (red marks) and FPRs (blue marks) for the *n*th center frequencies. The *y* axis is scaled with a log function.

designs [20,22], we introduce both HRs and FPRs as the low-frequency and high-frequency modulators, respectively. Furthermore, to combine these two elements in an integrated structure, the furcate channel is deliberately designed with an optimized geometry.

The modulators at the bottom and the top are used to control low frequencies (three center frequencies with $f_1 = 250$ Hz, $f_2 = 500$ Hz, and $f_3 = 1000$ Hz). The modulators in the middle are used to modulate high frequencies (four center frequencies with $f_4 = 2000$ Hz, $f_5 = 4000$ Hz, $f_6 = 8000$ Hz, and $f_7 = 16\,000$ Hz). Figure 2(b) illustrates the three-dimensional (3D) structure of the AMEQ. The filters for different center frequencies (f_n) are marked in the figure. Figure 2(c) shows the air channel, which is the complementary part of the solid structure in Fig. 2(b). Sound propagates in the air channel. Figure 2(d)

shows the whole 2D metastructure of the AMEQ. The box at the bottom shows an enlarged view of the solid box, showing the structural schematic diagram of each unit cell, with different geometric parameters marked in the figure. The blue structure corresponds to low frequencies. The corresponding filter structure is based on HRs with different sizes [29,30]. The red structure corresponds to high frequencies, and the corresponding filter structure is based on FPRs with different lengths [20,31]. The whole structure is symmetrical in the four quadrants [marked by *A*, *B*, *C*, and *D* in Fig. 2(c)], so each resonator has four identical duplicates in the panel. Figure 2(e) shows the effective circuit model of the AMEQ, which is an electrical element analogy [29,30] corresponding to the analytical derivations we present in the following section. The arrows indicate the input and output ports.

We achieve precise modulation of the transmitted amplitude by optimizing the resonant-frequency f_{nm} distributions of the different resonators as shown in Fig. 2(f), in which the y axis is scaled with log function. Red marks in Fig. 2(f) are the resonant frequencies f_{nm} of the mth HR unit cell of the nth ($n=1,\ 2,\ 3$) supercell contributing to the nth center frequency (f_n), while blue marks are the resonant frequencies f_{nm} of the mth FPR unit cell of the nth ($n=4,\ 5,\ 6,\ 7$) supercell contributing to f_n. For example, for the sixth center frequency ($n=6, f=8000$ Hz), six resonators are designed with resonant frequencies of $f_{61}=6400$ Hz, $f_{62}=7000$ Hz, $f_{63}=7640$ Hz, $f_{64}=8420$ Hz, $f_{65}=9040$ Hz, and $f_{66}=9720$ Hz to ensure the broadband feature, as the blue marks in Fig. 2(f) show. The whole structure formed by these resonant-frequency distributions can achieve precise modulation of the amplitude with desired values.

To theoretically approach the properties of our concept, we investigate the specific resonator design with analytical expressions. For low-frequency filters, a HR array is designed. As shown in Fig. 2(d), the three supercells of the HRs correspond to the three center frequencies (f_1–f_3), having three, four, and ten HRs, respectively. In principle, the center frequency for each filter band is the average of the resonant frequencies of different HRs, viz., $f_n=\bar{f}_{nm}$, ($n=1,\ 2,\ 3$). The resonant frequency of the HR is expressed as

$$f_{nm}=\frac{1}{2\pi}\sqrt{\frac{1}{M_{nm}C_{nm}}}, \tag{1}$$

where $M_{nm}=\rho_0 l_{nm}/w_{nm}$ and $C_{nm}=L_{nm}d_{nm}/\rho_0 {c_0}^2$ are acoustic masses and acoustic capacitances of the HR, respectively, where $\rho_0=1.21$ kg/m^3 and $c_0=343$ m/s are the mass density and the sound speed in air, respectively, L_{nm} and d_{nm} are the height and the width of the cavity as marked in Fig. 2(d), and l_{nm} and w_{nm} are the height and the width of the neck, respectively.

Then, the effective impedance of HRs in the effective-circuit model is calculated by [30,32]

$$Z_{nm}=i(\omega_{nm}M_{nm}-1/\omega_{nm}C_{nm})+R_{nm}, \tag{2}$$

where $\omega_{nm}=2\pi f_{nm}$ are the angular frequencies and R_{nm} is the acoustic resistance induced by effects of the radiation and thermal viscosity. R_{nm} can be formulated as

$$R_{nm}\approx\frac{8L_{nm}}{\pi {w_{nm}}^2}\sqrt{2\mu\omega_{nm}\rho_0}+8\frac{\sqrt{2\mu\omega_{nm}\rho_0}}{\pi w_{nm}}+\frac{4\rho_0 c_0}{\pi w_{nm}}\left[1-\frac{2J_1(k_{nm}w_{nm})}{k_{nm}w_{nm}}\right], \tag{3}$$

where $\mu=1.983\times10^{-5}$ Pa s is the dynamic viscosity of air and J_1 is the Bessel function of the first kind. Based on the effective-circuit model, we can explain the low-frequency acoustic filter as the result of sound reflection and the thermal-viscous loss (corresponding to the energy dissipation at ($R_n=\bar{R}_{nm}$) at the resonances of the HRs (corresponding to the resonances of the circuit branch).

After obtaining the acoustic impedance Z_{nm} for each individual HR, we can get the total effective impedance $Z(n)$ of the AMEQ for three different center frequencies.

$$Z(n)=\left(\sum_{m=1}^{M}\frac{1}{Z_{nm}}\right)^{-1},\quad n=1,\ 2,\ 3. \tag{4}$$

where M is total number of the HRs for the nth center frequency. On the other hand, for the high-frequency filters (red), an FPR array is designed. Similarly to the low-frequency structure, the center frequency for each high-frequency-filter band is the average of all resonant frequencies of different FPRs, $f_n=\bar{f}_{nm}$, ($n=4,\ 5,\ 6,\ 7$). The length and the width are h_{nm} and w_{nm}, respectively. The filter frequency of the FPR is expressed as [20]

$$f_{nm}=\frac{c_0}{4h_{nm}}. \tag{5}$$

The high-frequency acoustic filter is directly influenced by sound absorption in the FPR unit cells. On the other hand, the high-frequency acoustic filter is influenced by multiple sound reflections in the integrated metastructure. We characterize the high-frequency acoustic filter by acoustic resistance $R_n=\bar{R}_{nm}$ ($n=4,\ 5,\ 6,\ 7$) in the effective circuit. The effective impedance of FPRs is calculated by [20]

$$Z(n)=i\frac{\rho_0 c_0}{\omega}\left[\sum_{m=1}^{M}\frac{4\gamma\omega_{nm}}{(\omega_{nm}^2-\omega^2-i\beta\omega)(\pi M)}\right]^{-1},\quad n=4,\ 5,\ 6,\ 7, \tag{6}$$

where γ is the ratio of the surface area occupied by the FPR's cross sections to the effective surface area exposed

to sound, *M is* total number of the FPRs for the *n*th center frequency, and β describes the weak system dissipation for the acoustic metamaterial.

We can then modulate the transmission coefficient (acoustic pressure amplitude) by controlling the turned-on and turned-off states of each resonator using the modulators. Since each resonator has four identical duplicates in quadrants A, B, C, and D in the panel, the number of the activated (turned-on) resonators can be chosen as $\delta(n) = 0$, 1, 2, 3, or 4. Thus, on the basis of the effective acoustic impedance $Z(n)$, the transmission $T(n)$ of the AMEQ for the *n*th center frequencies is related to the value of $\delta(n)$, calculated as

$$T(n) = T_0, \quad \delta(n) = 0, \tag{7a}$$

$$T(n) = T_0\left[\frac{Z(n)}{Z(n)+\rho_0 c_0}\right], \quad \delta(n) = 1, \tag{7b}$$

$$T(n) = T_0\left[\frac{Z(n)-\rho_0 c_0}{Z(n)+\rho_0 c_0}\right], \quad \delta(n) = 2, \tag{7c}$$

$$T(n) = T_0\left[\frac{Z(n)[Z(n)-\rho_0 c_0]}{[Z(n)+\rho_0 c_0]^2}\right], \quad \delta(n) = 3, \tag{7d}$$

$$T(n) = T_0\left[\frac{Z(n)-\rho_0 c_0}{Z(n)+\rho_0 c_0}\right]^2, \quad \delta(n) = 4, \tag{7e}$$

where T_0 is the transmission of a pure channel without any resonators as shown in Fig. 3(a). Because the channel has an unusual shape, the transmission curve of T_0 is not planar, but is related to the working frequency, as shown in Fig. 3(b), with the averaged close to 0.8. Here we assume $T_0 = 0.8$ to simplify the following analytical calculations. From the curve of T_0, one can see the transmission above 1890 Hz is oscillating because it is the approximate cutoff frequency of the channel. Therefore, the low-frequency filters from 180 to 1890 Hz are due to the resonance of the whole structure. The high-frequency filters from 1890 to 22 000 Hz are determined by both the resonance of the FPR element and geometric acoustic effects. This is reflected in the parameter γ in Eq. (6), which is the effective filling rate related to the geometric feature of the channel and the distribution of FPRs. In this case, the filling rate γ is smaller than in the previous case for a compact structure [20].

B. Amplitude control

Owing to the precise modulation by the optimized resonator arrays, the transmitted amplitude is controlled with levels 0–4 corresponding to amplitudes $A = 0.8$, 0.63, 0.5, 0.4, and 0.3 (viz., −2, −4, −6, −8, and −10 dB, respectively). Figure 3(c) shows a schematic diagram for levels 0–4. In this diagram, the 28 circles represent 28 modulators for different f_n (each frequency has four tunable modulators). The red circles represent turned-off states, for which we fix a red slice covering the opening of the resonator to prevent the effect of the resonator. The gray circles represent turned-on states, indicating no slice is fixed. Photographs of the samples for levels 0–4 are also shown in Fig. 3(c). The sample is tunable by introduction of the red slices as modulators [33]. It has a size of $56 \times 56 \times 4$ cm^3 (the horizontal size of 56 cm is about one quarter of the wavelength of the lowest working frequency). The samples and the slices are made by a 3D printer with polylactic acid having mass density $\rho = 1250$ kg/m^3, Young's modulus $E = 3.2 \times 10^9$ Pa, and Poisson's ratio $\nu = 0.35$.

The simulations are performed using the commercial finite-element-analysis software program COMSOL MULTIPHYSICS 5.4a with the "Acoustic-Thermoviscous Acoustic Interaction, Frequency Domain" and "Thermoviscous Acoustic-Solid Interaction, Frequency Domain" modules. The mass density and the sound speed in background-medium air are $\rho_0 = 1.21$ kg/m^3 and $c_0 = 343$ m/s, respectively.

The simulated, analytical, and measured filter curves for five samples are shown in Fig. 3(c). The transmission for one center frequency, such as 8000 Hz, is obtained by our calculating the averaged acoustic pressure amplitude within one octave from 5657 to 11 314 Hz (with a step of 1/24 octave, viz., 25 frequencies). For the experiment, the measurements are performed in a 2D parallel-waveguide experimental system [33]. The distance between two parallel waveguides is 4 cm. The size of the parallel waveguides is 0.6×0.8 m^2. Sound-absorbing cotton is placed at the boundaries of the parallel waveguides to prevent undesired reflections. A 10-cm-diameter loudspeaker (matches with the input side size of 9.6 cm) is fixed at the input boundary of the sample. The acoustic wave is generated continuously and the static acoustic field is measured.

The output cross section of the sample is scanned to obtain the output average acoustic wave amplitude, with a 0.25-in.-diameter Brüel & Kjær type 4961 microphone and a Brüel&Kjær PULSE multichannel sound and vibration analyser type 3160. Brüel & Kjær software is used for measurement, in which "Constant Percentage Bandwidth Analyzer" is chosen so that the incident frequency is swept from 180 to 22 000 Hz. One can conveniently measure the averaged acoustic pressure amplitude in real time for every octave from $f_1 = 250$ Hz to $f_7 = 16\,000$ Hz. The results in Fig. 3(c) show that by controlling the number of modulators (0, 7, 14, 21, and 28, respectively), we can achieve a predesigned amplitude response (0.3–0.8) at the output side.

The analytical results agree with the simulated and experimental ones. The simulated amplitudes for 1000 and 2000 Hz are slightly higher than the predesigned ones. This

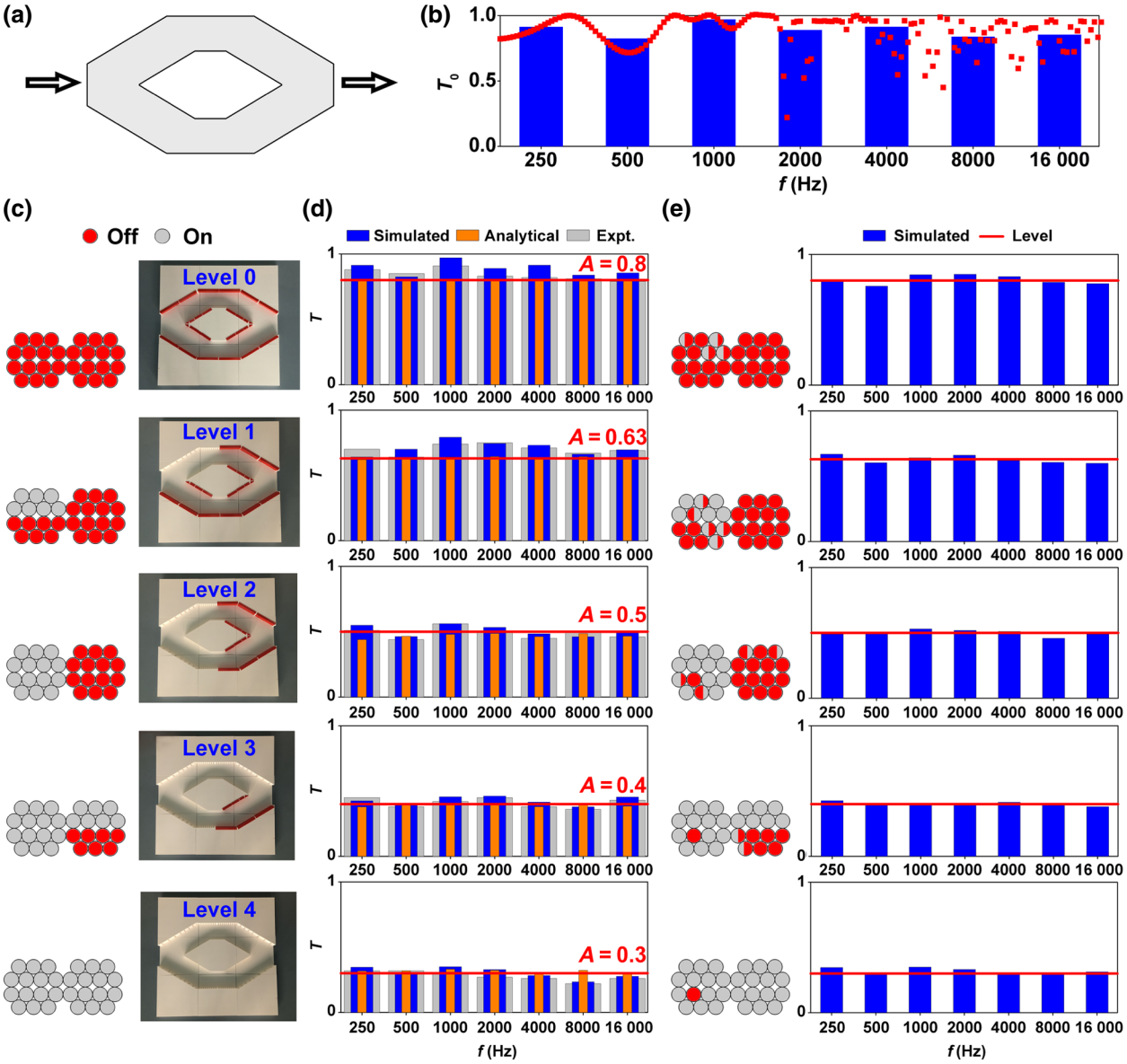

FIG. 3. Amplitude control. (a) The pure channel without any resonators. (b) Transmission of the pure channel without any resonators. The x axis is scaled with a log function. (c) Modulator distribution and photographs of the samples. (d) The simulated, analytical, and experimental results for the amplitude response at different octaves. The amplitude responses are modulated as levels 0–4 with $A = 0.8$, 0.63, 0.5, 0.4, and 0.3, respectively (-2, -4, -6, -8, and -10 dB respectively). The predesigned EQ values are represented by solid red lines. (e) The simulated results for the amplitude response at different octaves for the modified profiles.

is an inevitable error, and is because level 0 corresponds to the pure channel case, whose transmission T_0 is not exactly planar, as shown in Fig. 3(b), but has higher values around 1000–2000 Hz. One solution to further improve the amplitude curve is to use modified profiles of the activated modulators as shown in Fig. 3(e). The amplitude controls based on modified profiles are more precise. Anyhow, the results in Fig. 3(d) are already sufficient to show the ability of the proposed structure to control the sound transmission with specific values with small error for each targeted center frequency, respectively. The realization of the amplitude control is the foundation for other, more-complex acoustic equalization operations.

C. Functional filter

Different functional filters are important elements in signal processing [1], such as the classical ones (i.e., high-pass, low-pass, band-pass, and stop-band filters). In the following, we show the realization of the four aforementioned functional filters. A schematic diagram and the samples are shown in Figs. 4(a) and 4(d). The distributions

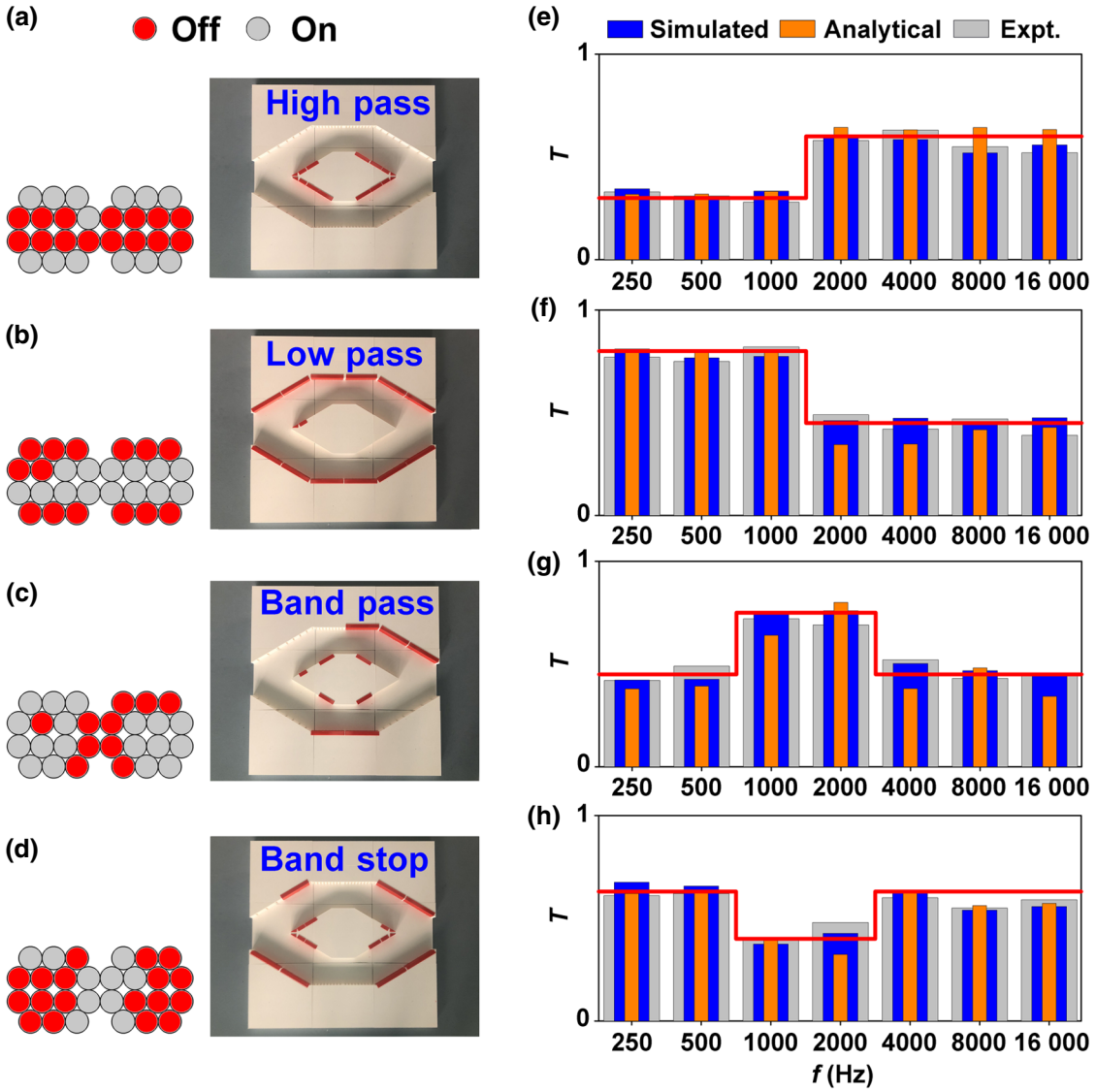

FIG. 4. Functional filter. (a)–(d) Modulator distribution and photographs of the samples. (e)–(h) Simulated, analytical, and experimental results for the samples for different functional filters, viz., high-pass, low-pass, band-pass, and band-stop filters, respectively. The predesigned EQ values are represented by solid red lines.

of the modulators are optimized to achieve the desired filter curve. The high-pass filter is designed as having high transmission for four octaves with center frequencies from 2000 to 16 000 Hz, while low transmission is designed for three octaves with center frequencies from 250 to 1000 Hz. In Fig. 4(e), the numerical and experimental results show that the amplitude response for 200–1400 Hz is about $A = 0.3$ and for 1400–20 000 Hz is about $A = 0.6$. Similar designs are applied to other filters in Fig. 4(f). The low-pass filter has $A = 0.8$ for 200–1400 Hz and $A = 0.45$ for 1400–20 000 Hz. The band-pass filter has a high-transmission band within two octaves (1000 and 2000 Hz) and has low transmission for the other octaves. In Fig. 4(g), the numerical, analytical, and experimental results show that the amplitude responses are approximately $A = 0.75$ for 700–2800 Hz and $A = 0.45$ for the other bandwidths (200–700 Hz and 2800–20 000 Hz). In contrast, the stop-band filter in Fig. 4(h) has a low-transmission band within two octaves (1000 and 2000 Hz) and has high transmission for the other octaves. The numerical and experimental results show that the amplitude responses are approximately $A = 0.35$ for 700–2800 Hz and $A = 0.65$ for other bandwidths (200–700 Hz and 2800–20 000 Hz). The realization of such functional filters will lead to applications in noise control with tunable frequency ranges.

D. Signal reproduction

Signal reproduction is an important concept proposed in room acoustics [8] that uses an equalization process

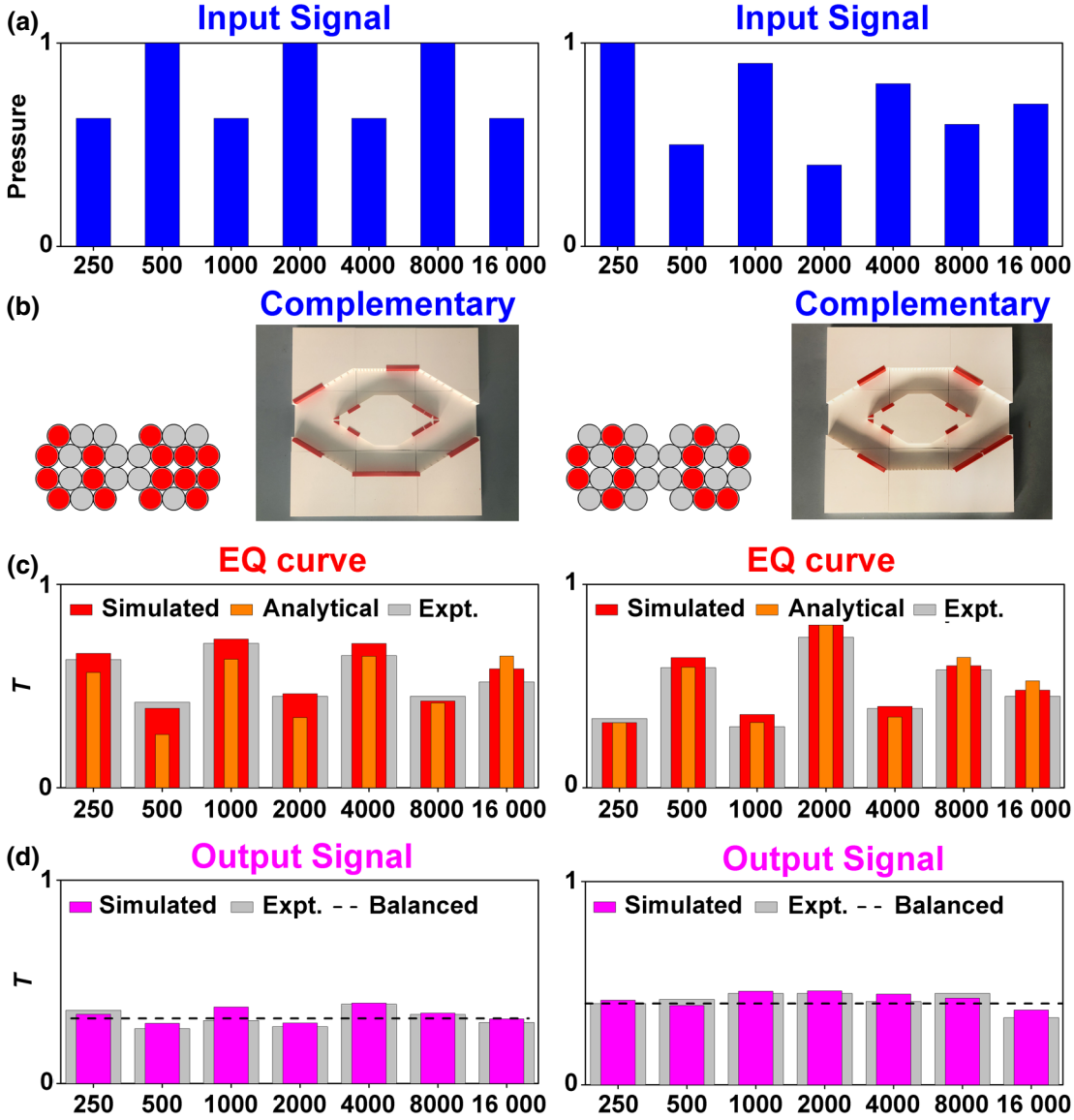

FIG. 5. Signal reproduction. (a) The input signals with unbalanced frequency amplitude ingredients. (b) Modulator distribution and photographs of the complementary samples. (c) Simulated, analytical, and experimental results for the EQ curve of samples for signal reproduction. (d) Simulated and experimental transmissions of output signals after the signal reproduction. The predesigned output values are represented by dashed black lines.

to reproduce the input signal with random or unbalanced frequency ingredients, and reconstructs it as a balanced one with a planar frequency-response curve. Figure 5(a) shows two examples of predesigned original incident signals (oscillating shapes) with unbalanced frequency ingredients, while Fig. 5(b) illustrates two optimized samples to reproduce the input signal. The frequency-response features of the samples need to be complementary to the input signals. Figure 5(c) summarizes simulated, analytical, and experimental EQ curves of the designed samples, which agree with the predicted complementary curves. These results are obtained by our comparing the output signal with a balanced input signal on the samples. Figure 5(b) shows the simulated and experimental results for sound reproduction, which are obtained by our comparing the output signal with the unbalanced input signals in Fig. 5(a). The numerical and experimental results evidence that the reproduced signal has a planar frequency response, showing the effectiveness of the optimized structures represented in Fig. 5(b) for signal reproduction.

E. Sound-effect control

Sound-effect control [5] is another fascinating application of an EQ device that requires a fine modulation of each frequency ingredient. We predesign four EQ curves

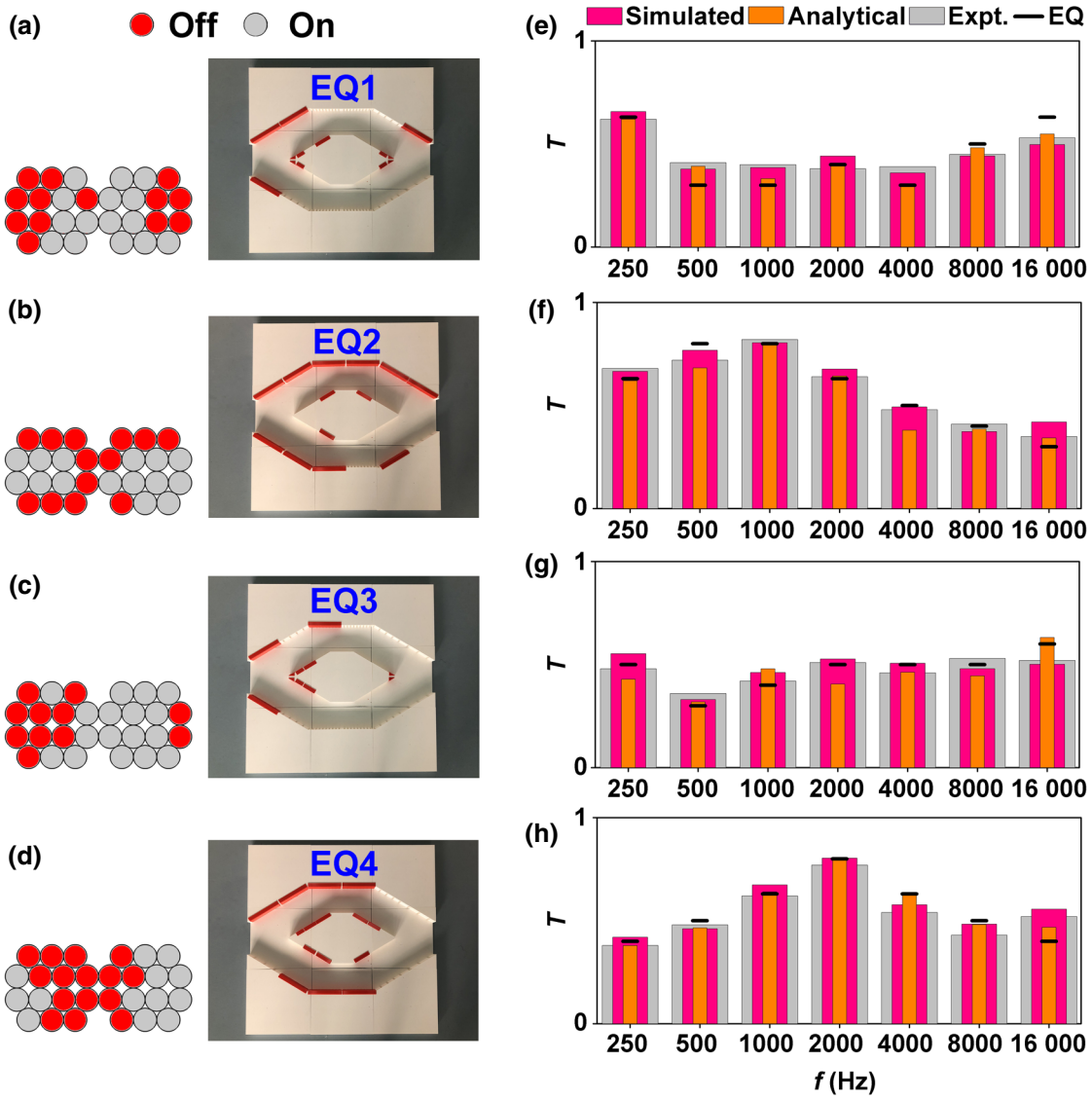

FIG. 6. Sound effect control. (a)–(d) Modulator distribution and photographs of the samples. (e)–(h) Simulated, analytical, and experimental results for the EQ curve of the samples for different sound effects, viz., EQ1 (hip-hop), EQ2 (popular), EQ3 (rhythm and blues), and EQ4 (dance), respectively. The predesigned EQ values are represented by a solid black line.

(denoted as EQ1–EQ4) whose sound effects are well known in music productions, viz., EQ1 (hip-hop), EQ2 (popular), EQ3 (rhythm and blues), and EQ4 (dance), respectively. The AMEQ structures as well as the simulated, analytical, and measured data are illustrated in Fig. 6. By optimizing the distribution of the modulators, we obtain the desired EQ curves at the output side of the AMEQ. The results show that the low-frequency control is more precise than the high-frequency control (such as the results at 16 kHz). This is because the high-frequency filter is more sensitive to the plane-wave incident waveform (direction). The ability of the AMEQ for real sound-effect control is significant for applications in architectural acoustics, when a high-quality hearing effect is desired.

III. DISCUSSION AND CONCLUSION

We propose the concept of an acoustic meta-equalizer capable of providing acoustic wave equalization with a passive acoustic metamaterial. The equalization requires a tunable and ultrabroadband frequency filter. By using two kinds of acoustic resonant unit cells (Helmholtz resonators and Fabry-Perot resonators), we realize ultrabroadband filters within a fully integrated structure. The optimization of the resonator design ensures highly precise amplitude modulation. The obtained bandwidth can reach seven octaves, viz., 200–20 000 Hz, while the amplitude can be modulated with five levels (−2 to −10 dB with a step of −2 dB), realized by our tuning 28 modulators. It is worth mentioning that the tunability of the current system

is manual via designed slices. To further improve the tunability of the system, a possible method is to introduce an origami structure [34] to switch the "turned-on" and "turned-off" states of the system by using folding slices. The bandwidth and the degree of freedom of the amplitude exceed those of conventional acoustic filters. In analogy with equalization applications in communication systems, room acoustics, and audio devices, we numerically and experimentally demonstrate and provide the proof of concept of functional filters, signal reproduction, and sound-effect control, respectively. The proposed concept of an acoustic meta-equalizer aims to connect acoustic metamaterials to practical acoustic applications. Although the precision of the proposed meta-equalizer is not as high as that of mature electronic counterparts, the proposed meta-equalizer may have unique applications in architectural acoustics. For example, a passive structure with an ultrabroadband feature is a good candidate for noise control with a controllable frequency spectrum. The concept of an equalizer extended from an electronic device to an acoustic metadevice will lead to more possible applications, such as noise control with ventilation property [35,36], beyond the applications of a conventional electronic equalizer.

ACKNOWLEDGMENTS

This work was supported by the Air Force Office of Scientific Research under Grant No. FA9550-18-1-7021 and by the Région Grand Est and Institut Carnot ICEEL.

[1] S. U. H. Qureshi, Adaptive equalization, Proc. IEEE **73**, 1349 (1985).
[2] D. Falconer, S. L. Ariyavisitakul, A. Benyamin-Seeyar, and B. Eidson, Frequency domain equalization for single-carrier broadband wireless systems, IEEE Commun. Mag. **40**, 58 (2002).
[3] https://en.wikipedia.org/wiki/Equalization.
[4] F. Everest, *The Master Handbook of Acoustics* (TAB Books, Blue Ridge Summit, 1981).
[5] D. Howard and J. Angus, *Acoustics and Psychoacoustics* (Focal, London, 1999).
[6] B. D. Radlovic, R. C. Williamson, and R. A. Kennedy, Equalization in an acoustic reverberant environment: Robustness results, IEEE Trans. Speech Audio Process. **8**, 311 (2000).
[7] F. Talantzis and D. B. Wardm, Robustness of multichannel equalization in an acoustic reverberant environment, J. Acoust. Soc. Am. **114**, 833 (2003).
[8] S. Spors, H. Buchner, R. Rabenstein, and W. Herbordt, Active listening room compensation for massive multichannel sound reproduction systems using wave-domain adaptive filtering, J. Acoust. Soc. Am. **122**, 354 (2007).
[9] S. M. Kuo and D. R. Morgan, *Active Noise Control Systems* (Wiley, New York, 1996).
[10] M. Bouchard, Multichannel affine and fast affine projection algorithms for active noise control and acoustic equalization systems, IEEE Trans. Speech Audio Process. **11**, 54 (2003).
[11] M. Stojanovic, J. Catipovic, and J. G. Proakis, Adaptive multichannel combining and equalization for underwater acoustic communications, J. Acoust. Soc. Am. **94**, 1621 (1993).
[12] M. Chitre, S. Shahabudeen, and M. Stojanovic, Underwater acoustic communications and networking: Recent advances and future challenges, Mar. Technol. Soc. J. **42**, 103 (2008).
[13] G. C. Ma and P. Sheng, Acoustic metamaterials: From local resonances to broad horizons, Sci. Adv. **2**, e1501595 (2016).
[14] S. A. Cummer, J. Christensen, and A. Alù, Controlling sound with acoustic metamaterials, Nat. Rev. Mater. **1**, 16001 (2016).
[15] Y. B. Xie, T. Tsai, A. Konneker, B. Popa, D. Brady, and S. A. Cummer, Single-sensor multispeaker listening with acoustic metamaterials, Proc. Natl. Acad. Sci. USA **112**, 10595 (2015).
[16] G. C. Ma, X. Y. Fan, P. Sheng, and M. Fink, Shaping reverberating sound fields with an actively tunable metasurface, Proc. Natl. Acad. Sci. USA **115**, 6638 (2018).
[17] Y. F. Zhu, J. Hu, X. D. Fan, J. Yang, B. Liang, X. F. Zhu, and J. C. Cheng, Fine manipulation of sound via lossy metamaterials with independent and arbitrary reflection amplitude and phase, Nat. Commun. **9**, 1632 (2018).
[18] C. Z. Shi, M. Dubois, Y. Wang, and X. Zhang, High-speed acoustic communication by multiplexing orbital angular momentum, Proc. Natl. Acad. Sci. USA **114**, 7250 (2017).
[19] X. Jiang, B. Liang, J. C. Cheng, and C. W. Qiu, Twisted acoustics: Metasurface-enabled multiplexing and demultiplexing, Adv. Mater. **30**, 1800257 (2018).
[20] M. Yang, S. Y. Chen, C. X. Fu, and P. Sheng, Optimal sound-absorbing structures, Mater. Horizons **4**, 673 (2017).
[21] B. Assouar, B. Liang, Y. Wu, Y. Li, J. C. Cheng, and Y. Jing, Acoustic metasurfaces, Nat. Rev. Mater. **1**, 460 (2018).
[22] Y. F. Zhu, X. D. Fan, B. Liang, J. C. Cheng, and Y. Jing, Ultrathin Acoustic Metasurface-Based Schroeder Diffuser, Phys. Rev. X **7**, 021034 (2017).
[23] T. Cox and P. D'Antonio, *Acoustic Absorbers and Diffusers: Theory, Design and Application* (Crc Press, New York, 2016).
[24] Y. Li and B. Assouar, Acoustic metasurface-based perfect absorber with deep subwavelength thickness, Appl. Phys. Lett. **108**, 063502 (2016).
[25] G. C. Ma, M. Yang, Z. Y. Yang, and P. Sheng, Low-frequency narrow-band acoustic filter with large orifice, Appl. Phys. Lett. **103**, 011903 (2013).
[26] Z. Q. Liu, H. Zhang, S. Y. Zhang, and L. Fan, An acoustic dual filter in the audio frequencies with two local resonant systems, Appl. Phys. Lett. **105**, 053501 (2014).
[27] B. Assouar, M. Senesi, M. Oudich, M. Ruzzene, and Z. L. Hou, Broadband plate-type acoustic metamaterial for low-frequency sound attenuation, Appl. Phys. Lett. **101**, 173505 (2012).
[28] G. Y. Song, Q. Cheng, B. Huang, H. Y. Dong, and T. J. Cui, Broadband fractal acoustic metamaterials for low-frequency sound attenuation, Appl. Phys. Lett. **109**, 131901 (2016).

[29] Y. F. Zhu and B. Assouar, Multifunctional acoustic metasurface based on an array of helmholtz resonators, Phys. Rev. B **99**, 174109 (2019).
[30] Y. F. Zhu and B. Assouar, Systematic design of multiplexed-acoustic-metasurface hologram with simultaneous amplitude and phase modulations, Phys. Rev. Mater. **3**, 045201 (2019).
[31] X. Jiang, B. Liang, R. Q. Li, X. Y. Zou, L. L. Yin, and J. C. Cheng, Ultra-broadband absorption by acoustic metamaterials, Appl. Phys. Lett. **105**, 243505 (2014).
[32] L. Kinsler, *Fundamentals of Acoustics* (Wiley, New York, 1982).
[33] S. W. Fan, S. D. Zhao, A. L. Chen, Y. F. Wang, B. Assouar, and Y. S. Wang, Tunable Broadband Reflective Acoustic Metasurface, Phys. Rev. Appl. **11**, 044038 (2019).
[34] Y. F. Zhu, F. Fei, S. W. Fan, L. Y. Cao, K. Donda, and B. Assouar, Reconfigurable Origami-Inspired Metamaterials for Controllable Sound Manipulation, Phys. Rev. Appl. **12**, 034029 (2019).
[35] T. Lee, T. Nomura, E. M. Dede, and H. Iizuka, Ultrasparse Acoustic Absorbers Enabling Fluid Flow and Visible-Light Controls, Phys. Rev. Appl. **11**, 024022 (2019).
[36] M. Sun, X. S. Fang, D. X. Mao, X. Wang, and Y. Li, Broadband Acoustic Ventilation Barriers, Phys. Rev. Appl. **13**, 044028 (2020).